JACS
JOURNAL OF THE AMERICAN CHEMICAL SOCIETY
Article
Cite This: J. Am. Chem. Soc. 2018, 140, 2575−2586
pubs.acs.org/JACS

Rhodamine-Platinum Diimine Dithiolate Complex Dyads as Efficient and Robust Photosensitizers for Light-Driven Aqueous Proton Reduction to Hydrogen

Guocan Li, Michael F. Mark, Hongjin Lv, David W. McCamant,* and Richard Eisenberg*

Department of Chemistry, University of Rochester, Rochester, New York 14627, United States

Supporting Information

ABSTRACT: Three new dyads consisting of a rhodamine (RDM) dye linked covalently to a Pt diimine dithiolate (PtN_2S_2) charge transfer complex were synthesized and used as photosensitizers for the generation of H_2 from aqueous protons. The three dyads differ only in the substituents on the rhodamine amino groups, and are denoted as **Pt-RDM1**, **Pt-RDM2**, and **Pt-RDM3**. In acetonitrile, the three dyads show a strong absorption in the visible region corresponding to the rhodamine $\pi-\pi^*$ absorption as well as a mixed metal-dithiolate-to-diimine charge transfer band characteristic of PtN_2S_2 complexes. The shift of the rhodamine $\pi-\pi^*$ absorption maxima in going from **Pt-RDM1** to **Pt-RDM3** correlates well with the HOMO−LUMO energy gap measured in electrochemical experiments. Under white light irradiation, the dyads display both high and robust activity for H_2 generation when attached to platinized TiO_2 nanoparticles (Pt-TiO_2). After 40 h of irradiation, systems containing **Pt-RDM1**, **Pt-RDM2**, and **Pt-RDM3** exhibit turnover numbers (TONs) of 33600, 42800, and 70700, respectively. Ultrafast transient absorption spectroscopy reveals that energy transfer from the rhodamine $^1\pi-\pi^*$ state to the singlet charge transfer (^{1}CT) state of the PtN_2S_2 chromophore occurs within 1 ps for all three dyads. Another fast charge transfer process from the rhodamine $^1\pi-\pi^*$ state to a charge separated (CS) $RDM^{(0\bullet)}$-$Pt^{(+\bullet)}$ state is also observed. Differences in the relative activity of systems using the RDM-PtN_2S_2 dyads for H_2 generation correlate well with the relative energies of the CS state and the PtN_2S_2 ^{3}CT state used for H_2 production. These findings show how one can finely tune the excited state energy levels to direct excited state population to the photochemically productive states, and highlight the importance of judicious design of a photosensitizer dyad for light absorption and photoinduced electron transfer for the photogeneration of H_2 from aqueous protons.

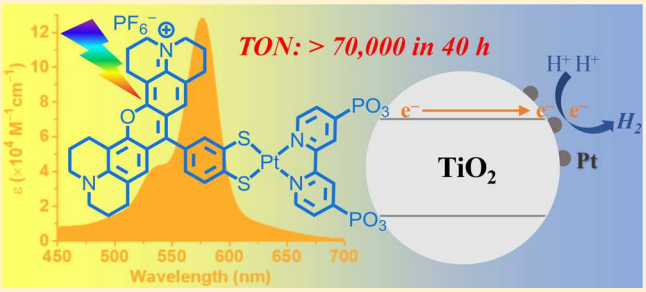

INTRODUCTION

Light-driven water splitting into hydrogen and oxygen represents a promising strategy for solar energy conversion to meet future global energy demand in an environmentally benign way.[1−4] As the most desirable reaction in artificial photosynthesis for storing solar energy in the form of chemical bonds, water splitting is a redox reaction that consists of water oxidation to O_2 and aqueous proton reduction to H_2. Due to the overall complexity of water splitting, it has generally been studied in terms of its two separate half-reactions.[5−12] During the past 30+ years, considerable progress has been made in terms of mechanistic understanding and catalyst design of each half-reaction through investigations involving sacrificial electron donors (SEDs) for H_2 generation and chemical oxidants for O_2 formation.[13−21] In this paper, we focus on the light-driven generation of H_2 from aqueous protons with a particular emphasis on the light-absorbing system to drive the reductive half-reaction.

Initial studies on light-driven H_2 generation described a multicomponent system consisting of $Ru(bpy)_3^{2+}$ (bpy = 2,2′-bipyridine) as the photosensitizer, methyl viologen (MV^{2+}) as the electron relay, a colloidal Pt catalyst, and a SED.[22−26] Subsequent studies by Grätzel determined that photoexcited $Ru(bpy)_3^{2+}$ was able to transfer an electron into TiO_2 so that platinized TiO_2 nanoparticles (Pt-TiO_2) were also able to produce H_2 in the presence of a chemical reductant.[27−29] In addition to $Ru(bpy)_3^{2+}$ and its Ru(II) trisdiimine analogues, metal complexes with long-lived triplet metal-to-ligand charge transfer (^{3}MLCT) excited states including Ir(III) d^6 phenylpyridine (ppy) complexes[30−32] and Pt(II) d^8 complexes such as $[Pt(tpy)(arylacetylide)]^+$ (tpy = terpyridine) were examined.[33−35] While these metal complexes were decent photosensitizers, they typically suffered from the major deficiency of high energy ^{1}MLCT absorptions (>2.6 eV, <480 nm) with low molar extinction coefficients (ε < ~15000 M^{-1} cm^{-1}).

Compared to the Ru(II), Ir(III) and Pt(II) complexes mentioned above, Pt(II) diimine dithiolate (PtN_2S_2) complexes are notable in having substantially lower-energy charge-transfer absorptions (610−650 nm), making them more interesting as potential photosensitizers for proton reduction.[36−39] Based on spectroscopic, electrochemical and computational results, the

Received: October 31, 2017
Published: February 8, 2018

DOI: 10.1021/jacs.7b11581
J. Am. Chem. Soc. 2018, 140, 2575−2586

HOMO (highest-occupied molecular orbital) in PtN_2S_2 complexes has mixed contributions from both Pt and dithiolate orbitals, while the LUMO (lowest-unoccupied molecular orbital) is diimine ligand-based.[36] The charge-transfer absorption in the PtN_2S_2 complexes is thus a mixed metal−ligand-to-ligand′ charge transfer (MMLL′CT). While more desirable energetically, the ^{1}MMLL′CT absorption in PtN_2S_2 complexes still suffered from low molar absorptivity (ε < ∼ 10000 $M^{-1}cm^{-1}$). Two PtN_2S_2 complexes coupled with Pt-TiO_2 exhibited decent stability under visible light irradiation (λ > 450 nm), but very limited TONs toward H_2 generation were obtained due to the weak absorptions.[40]

In contrast to the weak absorption of inorganic chromophores, the molar extinction coefficients of some organic dyes are an order of magnitude higher (∼10^5 M^{-1} cm^{-1}), such as Bodipy ((dipyrromethene)difluoroborate), Rose Bengal, Rhodamine B, Fluorescein, etc.[41−43] However, the absorptions of these organic dyes are usually $\pi-\pi^*$ centered and lacking charge-transfer character. In addition, the organic dyes tend to undergo photodecomposition under prolonged illumination. One strategy to take advantage of both the strong absorptivity of the organic dye and the charge-transfer character of PtN_2S_2 complexes is to covalently link them and use the organic dye as an antenna to transfer the absorbed energy to the low-energy ^{1}MMLL′CT transition. Following this strategy, Lazarides et al. reported a **Pt-Bodipy** dyad (R = H), in which a Bodipy dye is linked with PtN_2S_2 complex.[44,45] Further modification of the bipyridine ligand with diethyl-phosphate groups for binding to TiO_2 led to a **Pt-Bodipy**/Pt-TiO_2 system that exhibited significantly improved H_2 generation activity relative to PtN_2S_2 complex without Bodipy under green light irradiation (λ = 520 nm).[46,47]

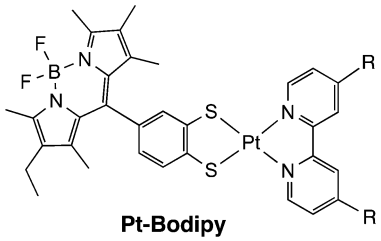

Pt-Bodipy

R = H, P(O)(OEt)$_2$

Despite the success of the **Pt-Bodipy**/Pt-TiO_2 system in the photogeneration of H_2 from aqueous protons, it had several drawbacks that impeded further improvement. The narrow $\pi-\pi^*$ absorption of Bodipy only absorbed the green fraction of visible light with moderate efficiency (ε ∼ 60000 $M^{-1}cm^{-1}$) and the long-term stability of the **Pt-Bodipy** dyad was questionable as the H_2 production activity dropped substantially at later stages of the experiment.[46] A photosensitizer with a wider and stronger absorption profile and greater stability appeared to be highly desirable. In this paper, we describe the synthesis, characterization and H_2-generating studies of three rhodamine-PtN_2S_2 dyads shown as **Pt-RDM1**, **Pt-RDM2**, and **Pt-RDM3** that differ only in the substituents on the rhodamine amino groups (Figure 1). These dyads possess significantly broader and enhanced absorptions compared to **Pt-Bodipy**. Under white light irradiation, these dyads when attached to Pt-TiO_2 exhibit substantially higher rates and robustness for H_2 generation from aqueous protons. The systematically varied **Pt-RDM** dyads are also studied by ultrafast transient absorption spectroscopy to correlate their relative activities and effectiveness in H_2 generation with the excited state dynamics to highlight the importance of avoiding an unwanted low-energy CS state for the development of more efficient photosensitizers for light-driven H_2 generation.

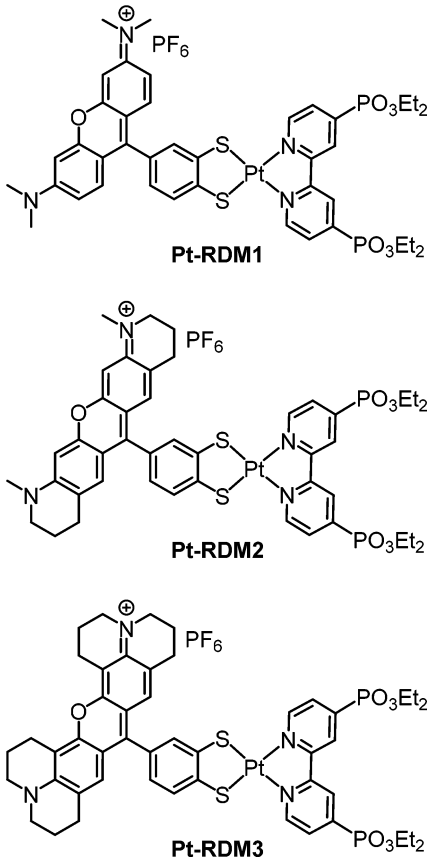

Figure 1. Molecular structure of **Pt-RDM1**, **Pt-RDM2**, and **Pt-RDM3**.

RESULTS

Syntheses. To date, rhodamines have enjoyed wide applications as imaging agents, sensors, and laser dyes,[48−50] but their use as light-harvesting antennae in dyad systems remains underexplored. This may be due to challenges associated with the synthesis of these dyes, especially as part of dyad and multicomponent light absorbers. The synthesis of rhodamine dyes generally involves a condensation reaction between an aldehyde substrate and two equivalents of 3-aminophenol derivatives under strong acidic condition.[51,52] However, the synthesis often suffers from low yields and difficulties in purification process. In the present study, the syntheses shown in Scheme 1 were carried out in 60% H_2SO_4 following modification of the procedure reported by Burgess.[53] That procedure employed microwave radiation, but in our case, simple heating of the reaction solution worked well for the preparation of **RDM1**, **RDM2**, and **RDM3** with yields ranging from 35% to 80%. Because rhodamine dyes are cationic, they are isolated as salts, the anion of which is sometimes ambiguous as a consequence of both synthesis and workup steps.[53] In purification of the rhodamine dyes by column chromatography, we observed several bright orange/red fractions that were intermixed and essentially inseparable. Initially regarded as a mixture of product and impurities, they were later identified as the desired rhodamine dye with different anions. An anion exchange reaction using NH_4PF_6 in methanol led successfully

DOI: 10.1021/jacs.7b11581
J. Am. Chem. Soc. 2018, 140, 2575−2586

Scheme 1. Synthetic Procedure to Prepare Pt-RDM1, Pt-RDM2, and Pt-RDM3[a]

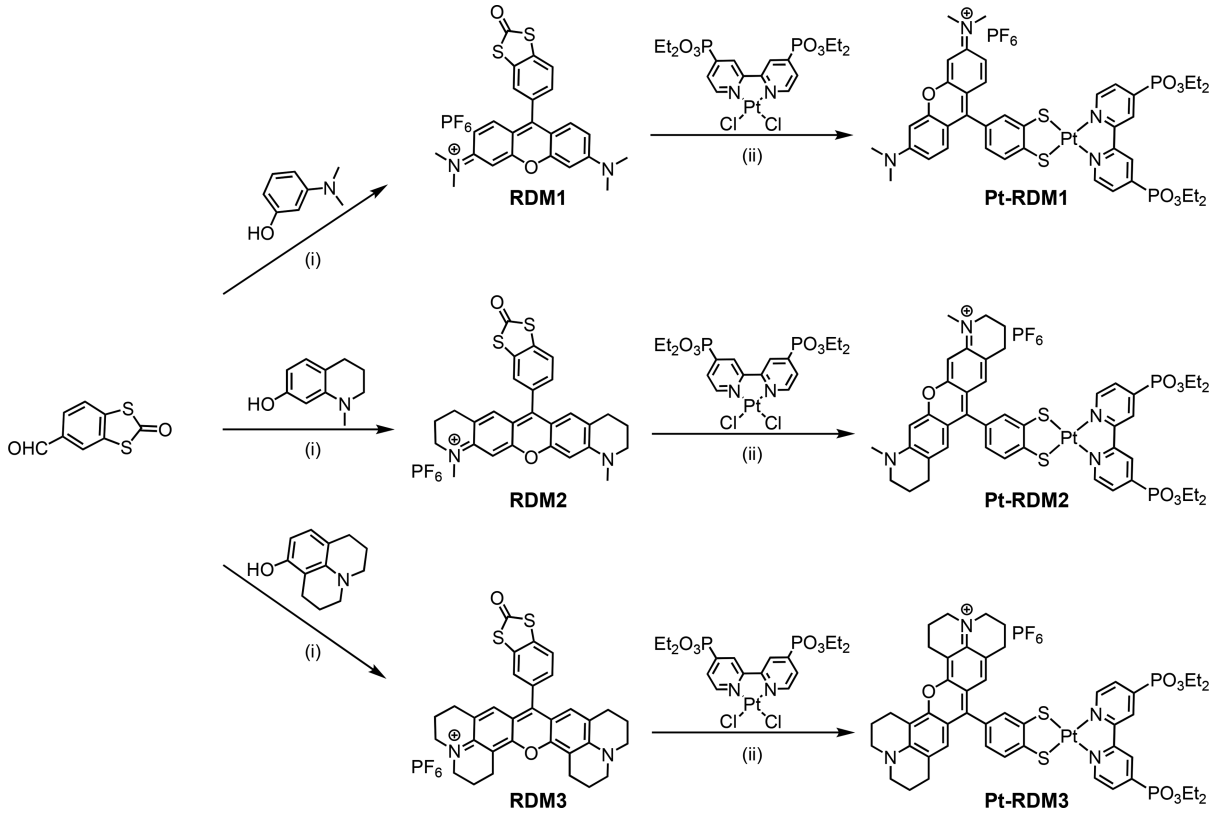

[a](i) 60% H_2SO_4, 85 °C, 18 h; *p*-chloranil, RT, 1 h; NH_4PF_6, 3 equiv. (ii) Potassium *tert*-butoxide, MeOH, RT, 24 h.

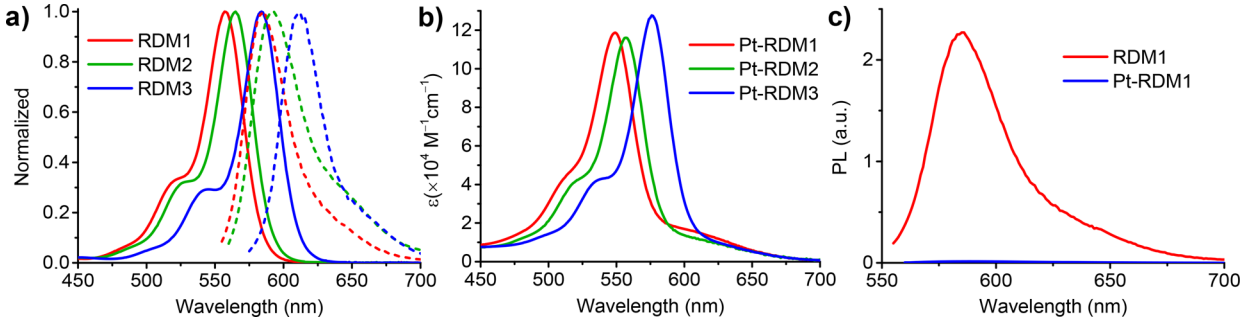

Figure 2. (a) Normalized absorption (solid line) and fluorescence (dashed line) spectra of **RDM1**, **RDM2**, and **RDM3** in acetonitrile. (b) Absorption molar extinction coefficient of **Pt-RDM1**, **Pt-RDM2**, and **Pt-RDM3** in acetonitrile. (c) Fluorescence of **Pt-RDM1** relative to **RDM1** in acetonitrile when excited at 540 nm at room temperature.

to isolation of the desired product as the PF_6^- salt. Reaction of the corresponding rhodamines with potassium tert-butoxide and $Pt(Pbpy)Cl_2$ in MeOH for 24 h at room temperature produced the desired dyads **Pt-RDM1**, **Pt-RDM2**, and **Pt-RDM3** in moderate-to-good yields. Elemental analyses, mass spectrometry, and ^{1}NMR spectra (Figures S1 and S2) of the isolated compounds are fully consistent with their formulations in Scheme 1.

Photophysical Properties. Rhodamine dyes **RDM1−3** exhibit a strong $\pi-\pi^*$ absorption (~10^5 M^{-1} cm^{-1}) in the yellow−orange region of the visible spectrum along with a higher energy vibronic shoulder (Figure 2a). A red shift of the absorption maxima is observed for **RDM2** and **RDM3** relative to **RDM1** (7 nm shift for **RDM2** and 26 nm shift for **RDM3**). The dyes are strong fluorophores with fluorescence quantum yields ranging from 0.7 to unity in acetonitrile (Figure S4 and Table 1). The greater fluorescence quantum yields for **RDM2** and **RDM3** may arise from the restricted rotation of the amino

Table 1. Photophysical Properties of Dyes RDM1−3 and Dyads Pt-RDM1−3 in Acetonitrile

compd	Abs_{max}, nm	ε, M^{-1} cm^{-1}	Fl_{max}, nm[a]	ϕ_{Fl}[a]	Ph_{max}, nm[b]
RDM1	558	99700	585	0.7	N/A
RDM2	565	93000	592	1.0	N/A
RDM3	584	119000	611	1.0	N/A
Pt-RDM1	549	119000	587	0.004	696,[c] 761[d]
Pt-RDM2	557	116000	590	0.01	716,[c] 765[d]
Pt-RDM3	576	128000	600	0.006	745,[c] 759[d]

[a]Measured at room temperature. [b]Measured at 77 K in EtOH/MeOH = 4:1 optical glass. [c]Excited at 550 nm. [d]Excited at 650 nm.

DOI: 10.1021/jacs.7b11581
J. Am. Chem. Soc. 2018, 140, 2575−2586

alkyl groups. A 27 nm Stokes shift is observed in the fluorescence for all three rhodamines relative to the corresponding absorption. None of the rhodamine dyes **RDM1−3** exhibit observable phosphorescence at room temperature or 77 K.

The **Pt-RDM1** dyad exhibits two main absorptions in acetonitrile solution, including an intense rhodamine $\pi-\pi^*$ transition at 549 nm ($>10^5$ M^{-1} cm^{-1}) and a broad ^{1}MMLL′CT absorption around 600 nm (Figure 2b). The other dyads, **Pt-RDM2** and **Pt-RDM3**, show similar absorption features as **Pt-RDM1**, except for a red shift of the rhodamine $\pi-\pi^*$ absorption as observed for the rhodamine dyes, while the ^{1}MMLL′CT absorption remains unmoved. Relative to the parent rhodamines, there is an 8 nm shift to higher energy for the rhodamine $\pi-\pi^*$ transitions in the dyads. In the dyads, the rhodamine $\pi-\pi^*$ absorption overlaps significantly with the ^{1}MMLL′CT band, especially in **Pt-RDM3**, in which only a tail of the charge transfer band is observable. These two transitions in the dyads are better resolved in dichloromethane due to the bathochromic shift of the ^{1}MMLL′CT absorption that is well-known for the PtN_2S_2 chromophore (Figure S3).[36] In contrast to the strong fluorescence of rhodamines, the fluorescence of the corresponding dyads is significantly quenched (Figures 2c, S4, and S5), consistent with the notion of efficient energy transfer from the rhodamine $^1\pi-\pi^*$ excited state to the PtN_2S_2 ^{1}MMLL′CT state. No phosphorescence is observed for the **Pt-RDM** dyads at room temperature. At 77 K, **Pt-RDM** dyads display both rhodamine-centered fluorescence and phosphorescence when excited at 550 nm.[54] The phosphorescence from the rhodamine $^3\pi-\pi^*$ excited state is situated at lower energy relative to the fluorescence, and red-shifts progressively from 696 nm in **Pt-RDM1** to 745 nm in **Pt-RDM3** (Figure S6). When excited at 650 nm to the ^{1}MMLL′CT state at 77 K, all three **Pt-RDM** dyads exhibit PtN_2S_2-centered phosphorescence at ∼760 nm from the ^{3}MMLL′CT state.

Electrochemical Properties. The electrochemical properties of the rhodamine dyes **RDM1−3** and the rhodamine-PtN_2S_2 dyads **Pt-RDM1−3** were assessed by cyclic voltammetry in acetonitrile (Table 2). **RDM1** displays two reversible redox processes, an oxidation at 1.50 V and a reduction at −0.46 V vs NHE (Figure 3a). A second irreversible reduction process is also present (Figure S7a). Relative to the redox processes in **RDM1**, the corresponding redox processes in **RDM2** and **RDM3** occur at increasingly negative potentials with a larger shift for the oxidation than the reduction. As a result, the potential gap between the reversible oxidation and reduction decreases progressively from 1.96 V in **RDM1** to 1.92 V in **RDM2**, and 1.84 V in **RDM3**. The potential gap reflects qualitatively the energy gap between HOMO and LUMO and is linearly correlated with the absorption and fluorescence maxima (Figure S7b). It is also consistent with the lower energy absorption and fluorescence maxima seen for **RDM2** and **RDM3** relative to **RDM1**. The negative shift of the potentials in **RDM2** and **RDM3** is thought to be related to the structural changes in the rhodamine dyes. Unlike the free amino methyl groups in **RDM1**, the electron-donating amino alkyl groups in **RDM2** and **RDM3** are covalently linked to the xanthene core, making the rhodamine more susceptible to oxidation and more difficult to reduce.

Table 2. Electrochemical Potentials of Dyes RDM1−3 and Dyads Pt-RDM1−3 in Acetonitrile

compd	$E_{1/2}^{ox1}$, V	$E_{1/2}^{ox2}$, V	$E_{1/2}^{red1}$, V	$E_{1/2}^{red2}$, V
RDM1	1.50	N/A	−0.46	−1.08[a]
RDM2	1.31	N/A	−0.61	−1.20[a]
RDM3	1.15	N/A	−0.69	−1.32[a]
Pt-RDM1	1.46	1.01[a]	−0.60	−0.71
Pt-RDM2	1.31	1.01[a]	−0.70	−0.70
Pt-RDM3	1.19	1.01[a]	−0.70	−0.75

[a]The peak potential is reported due to irreversibility.

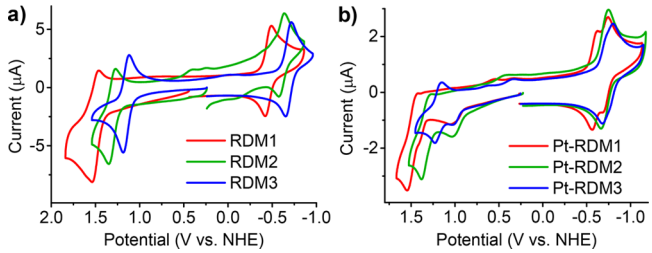

Figure 3. Cyclic voltammograms of (a) **RDM1−3** and (b) **Pt-RDM1−3** measured in 0.1 M $TBAPF_6$ acetonitrile solution. Scan rate = 0.1 V/s.

The dyads **Pt-RDM1−3** exhibit a total of four redox processes within the acetonitrile electrochemical window. In addition to the rhodamine centered oxidation and reduction, an additional irreversible Pt-centered oxidation and reversible bipyridine-centered reduction are present (Figure 3b), in accord with the earlier report of the PtN_2S_2 chromophore.[36] The redox potentials for both the Pt-centered oxidation and bipyridine-centered reduction are essentially unchanged for **Pt-RDM1−3** and remain at 1.01 V and −0.70 V (vs NHE), respectively. The rhodamine-centered redox processes in the dyads show the same negative shift from **Pt-RDM1** to **Pt-RDM3** as observed in the parent rhodamine dyes.

Despite the change in oxidation potentials, rhodamine oxidation is always preceded by the oxidation of Pt for the three dyads. In contrast, the change in **RDM** reduction potentials causes the rhodamine reduction to cross the bipyridine reduction from **Pt-RDM1** to **Pt-RDM3**. As shown in Figure 3b, in **Pt-RDM1**, these two reversible reductions are well distinguished, with the **RDM1** reduction at −0.60 V and the bpy reduction at −0.71 V. In **Pt-RDM2**, these two reductions completely overlap with each other and appear at −0.70 V. Further negative shift of rhodamine reduction in **Pt-RDM3** causes the rhodamine reduction wave to become more negative than the bipyridine reduction, resulting in the shoulder that reappears at −0.75 V. The redox potentials for the two reductions in **Pt-RDM3** was determined by differential pulse voltammetry. The relative shifts in rhodamine reduction potentials are important in analyzing dyad effectiveness for the photogeneration of H_2 (vide infra).

Light-Driven H_2 Generation. The **Pt-RDM1−3** dyads were attached on Pt-TiO_2 nanoparticles to assess their ability to promote H_2 production. The method of attachment involved sonication of 2.5 mL of X μM (X = 10, 50) acetonitrile solutions of **Pt-RDM1−3** dyads in the presence of 20 mg Pt-TiO_2 nanoparticles during which diethyl phosphonate ester hydrolysis and dyad binding to the nanoparticles occur. The dyad-attached Pt-TiO_2 nanoparticles were collected by centrifugation and mixed with 5 mL of 0.5/1.0 M AA aqueous solution at pH = 4.0 for photochemical H_2 production (Figure S9). The absorption of the supernatant solution was measured

DOI: 10.1021/jacs.7b11581
J. Am. Chem. Soc. 2018, 140, 2575−2586

to estimate the amount of dyad attached to the nanoparticles. A commercially available white light LED was used as the light source. The H_2 production activity was monitored in real-time using a pressure transducer fitted on the top of the vial, and the amount of H_2 produced was quantified with gas chromatography (GC) after the photolysis using CH_4 as an internal standard (Figures S10 and S12).

When X = 50 μM, about 99% dye attachment was achieved after sonication (Figure S8). The photochemical H_2 production experiment was performed in 5 mL 0.5 M AA aqueous solution. The three dyad-systems **Pt-RDM1−3**/Pt-TiO_2 exhibit notable activity in the photogeneration of H_2 at pH = 4.0 (Figure 4). In

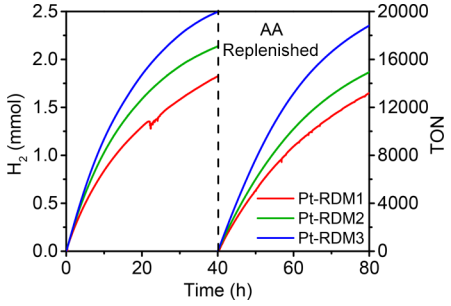

Figure 4. Light generated hydrogen production using systems containing 2.5 mL 50 μM dyads **Pt-RDM1−3** as photosensitizers on 20 mg Pt-TiO_2 nanoparticles in 5 mL of 0.5 M AA aqueous solution (pH = 4.0).

40 h of white-light irradiation, 43.2, 52.5, and 60.0 mL H_2 corresponding to 1.8, 2.1, and 2.5 mmol H_2 were produced by the respective dyad systems **Pt-RDM1−3**/Pt-TiO_2, giving turnover numbers (TON) of 14600, 17100, and 20000 (Table 3) with respect to the dye. It has been established

Table 3. Hydrogen Production Activity and Parameters for Systems Containing 2.5 mL of 50 μM Pt-RDM1−3 Dyads on 20 mg Pt-TiO_2 Nanoparticles

compd	attachment %	AA, M	time, h	H_2, mmol	TON_{dye}
Pt-RDM1	99%	0.5	40	1.8	14400
			40−80	1.7	13200
Pt-RDM2	99%		40	2.1	17100
			40−80	1.9	14900
Pt-RDM3	99%		40	2.5	20000
			40−80	2.4	18800
Pt-RDM1	87%		40	3.2	29700
			40−80	2.4	22500
Pt-RDM2	97%	1.0	40	4.4	35900
			40−80	2.7	21900
Pt-RDM3	97%		40	5.0	40000
			40−80	4.1	32400

that the singly oxidized deprotonated AA$^{\bullet}$ undergoes disproportionation reaction to form AA and dehydroascorbic acid (DHA),[55,56] therefore each AA can provide two electrons for H_2 production. In the case of **Pt-RDM3**, all the AA was consumed for H_2 production.

After 40 h of irradiation, the rates of H_2 generation decreased substantially for all systems due to AA consumption as the sacrificial electron donor. The spent AA solution was removed following centrifugation and 5 mL 0.5 M fresh AA aqueous solution was added to each system, which led to a resumption of activity in H_2 evolution for the **Pt-RDM1−3**/TiO_2 dyad systems that approached their respective initial rates (Figure 4). Over the next 40 h, these systems exhibited activity for H_2 production that mirrored their performance during the initial 40 h period with only modest declines in the overall rates (8%, 13%, 6%, respectively). Over the 80-h irradiation period, total TONs of 27600, 32000, and 38800 were found for the systems containing **Pt-RDM1**, **Pt-RDM2**, and **Pt-RDM3**, respectively.

In light of the fact that all the AA was consumed by **Pt-RDM3** when 5 mL of 0.5 M AA was used, the concentration of AA was raised to 1.0 M while keeping the pH at 4.0. Under white light irradiation for 40 h, the **Pt-RDM1−3**/Pt-TiO_2 systems generated so much H_2 that it exceeded the threshold of the pressure transducer. After 40 h of irradiation, 3.2, 4.4, and 5.0 mmol H_2 were produced by **Pt-RDM1−3**/Pt-TiO_2 system, corresponding to a TON of 29700, 35900, and 40000 for **Pt-RDM1**, **Pt-RDM2**, and **Pt-RDM3**, respectively. The aqueous solution turned from colorless to yellow after the photolysis due to the accumulation of DHA (Figure S11a). The aqueous solution corresponding to **Pt-RDM3** exhibited the strongest absorption due to the highest DHA concentration (Figure S11b), which was consistent with its largest TON. Compared to the TONs in the presence of 0.5 M AA, the TON for **Pt-RDM1** and **Pt-RDM2** increased by more than 100% when 1.0 M AA was present (Table 3). In the case of **Pt-RDM3**, all the AA was fully consumed again despite the increase of AA concentration. After 40 h of irradiation, the AA solution was replenished with 5 mL of 1.0 M fresh AA aqueous solution, and the **Pt-RDM1−3**/Pt-TiO_2 systems continued to actively generate H_2 under white light irradiation. Over the next 40 h, **Pt-RDM1−3**/Pt-TiO_2 system managed to maintain 76%, 61%, and 81% of the initial TONs, giving rise to a total respective TON of 52200, 57800, and 72400 for **Pt-RDM1**, **Pt-RDM2**, and **Pt-RDM3** over 80 h of irradiation (Table 3).

Given the truly notable activity of these dyads, the dye loading was reduced by 80% by using 2.5 mL of 10 μM dyad acetonitrile solutions for dye attachment. UV−vis absorption of the supernatant suggested all the dyad were successfully adsorbed on Pt-TiO_2 nanoparticles. In the presence of 5 mL of 1.0 M AA aqueous solution (pH = 4.0), 0.8, 1.1, and 1.8 mmol H_2 was produced by **Pt-RDM1−3**/Pt-TiO_2 system over 40 h of white light irradiation, corresponding to a respective TON of 33600, 42800, and 70700 for **Pt-RDM1**, **Pt-RDM2**, and **Pt-RDM3** (Figures 5 and S12). The solution absorption after the photolysis due to the generation of DHA is fully consistent with the order of the TON for the three dyads (Figure S13).

To date, a number of organic and inorganic photosensitizers have been used in combination with Pt-TiO_2 for light-driven generation of H_2, including Ru(II) polypyridyl complexes,[57] [Pt(tpy)(arylacetylide)] type complexes,[33,47] selenorhodamine,[58] anthraquinone dye,[59] donor-π-acceptor type dyes,[60] etc. Among all the reported molecular photosensitizers, **Pt-RDM3** exhibits the highest TON for light-driven generation of H_2.

Compared to the **Pt-Bodipy** dyad, the **Pt-RDM** dyads exhibit significantly improved activity and stability for H_2 production.[46] The improved performance most certainly arises from the enhanced absorptivity of **Pt-RDM1−3**. The broader and stronger absorption of the **Pt-RDM** dyads allows harvesting more photons over the irradiation period, thus supplying more injected electrons from the excited states for proton reduction. The enhanced stability of **Pt-RDM1−3** is closely related to the

DOI: 10.1021/jacs.7b11581
J. Am. Chem. Soc. 2018, 140, 2575−2586

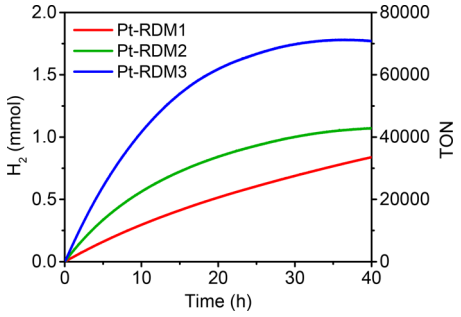

Figure 5. Light generated hydrogen production using systems containing 2.5 mL of 10 μM dyads **Pt-RDM1−3** as photosensitizers on 20 mg Pt-TiO_2 nanoparticles in 5 mL of 1.0 M AA aqueous solution (pH = 4.0).

stability of rhodamine under experimental conditions at pH = 4.0. Rhodamines are strongly resistant to acidic conditions,[48,61] as the conditions of their synthesis attest (see above).

Ultrafast Transient Absorption. Ultrafast transient absorption studies were undertaken to provide insight into the causes of the relative effectiveness of the **Pt-RDM** dyads. All three dyads and the parent rhodamine dyes were examined and showed similar excited-state dynamics. The excited state dynamics of **RDM3** and **Pt-RDM3** will be discussed in detail and those of **RDM1**, **RDM2**, **Pt-RDM1**, and **Pt-RDM2** can be found in the Supporting Information. In Figure 6, the transient

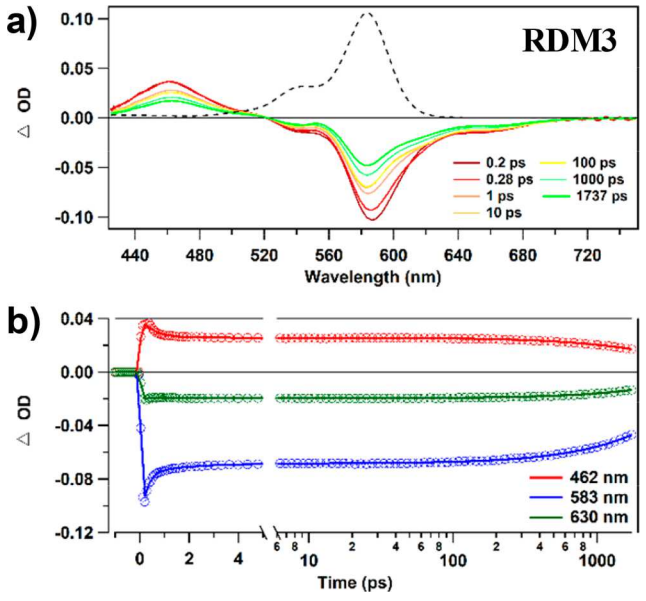

Figure 6. (a) TA spectra of **RDM3** at indicated time delays, and (b) kinetic traces of **RDM3** at selected wavelength, in acetonitrile after pulsed laser excitation at 550 nm.

absorption spectra (TA spectra) and single wavelength kinetics for **RDM3** are shown. The TA spectra of **RDM3** show a ground state bleach (GSB) (550−580 nm) of rhodamine absorption, a stimulated emission (SE) appearing at the low-energy side of the bleach (570−680 nm), and an excited state absorption (ESA) that appears around 440−460 nm. After an ultrafast solvent reorganization and vibrational cooling, the RDM $^1\pi-\pi$ excited state decays back to the ground state with a lifetime of several nanoseconds that exceeds the temporal window of our instrumental setup (Figure 6b). The presence of an isosbestic point with ΔOD = 0 around 520 nm (Figure 6a) is consistent with simple $^1\pi-\pi^*$ to ground-state relaxation dynamics and the absence of additional pathways in the decay of the excited state population.

Figure 7 shows the TA spectra of **Pt-RDM3** dyad after 650 nm laser excitation to the ^{1}MMLL′CT state. Immediately upon

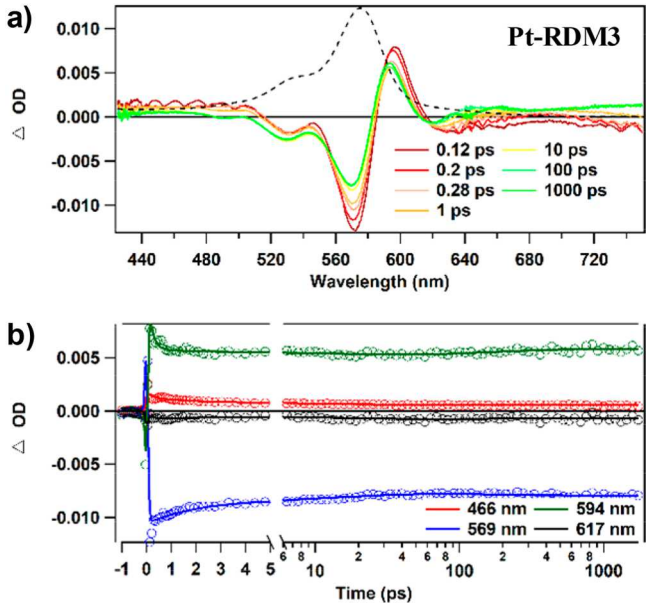

Figure 7. (a) TA spectra of **Pt-RDM3** at indicated time delays, and (b) kinetic traces of **Pt-RDM3** at selected wavelengths, in acetonitrile after pulsed laser excitation at 650 nm.

photoexcitation, a GSB appears at 620−660 nm, along with a prominent dispersive feature that shows up at 540−620 nm, which is consistent with a red-shift of the **RDM3** ground state absorption due to a nearby large excited-state dipole emanating from the ^{1}MMLL′CT excited state.[45] Global kinetic fits reveal two time constants for excited state relaxation, 1.9 and 21.1 ps, which are attributed to ISC from ^{1}MMLL′CT to the ^{3}MMLL′CT state and subsequent vibrational relaxation, respectively. After ∼20 ps, the spectrum remains roughly constant for the duration of the experiment, consistent with the long-lived nature of the ^{3}MMLL′CT state.

Upon 550 nm pulsed laser excitation to the rhodamine $^1\pi-\pi^*$ excited state, the **Pt-RDM3** dyad shows an instantaneous TA spectrum that resembles that of free **RDM3** (Figure 8a). The initially formed TA spectrum undergoes an ultrafast reorganization in <1 ps. On the same time scale, singlet energy transfer (SEnT) from the rhodamine $^1\pi-\pi^*$ to the PtN_2S_2 ^{1}MMLL′CT state takes place, evident in the loss of the rhodamine GSB and SE along with the appearance of a new GSB of the ^{1}MMLL′CT absorption at 600−670 nm. Global kinetic fits (Figure 8b) indicate that the ultrafast reorganization, SEnT, and subsequent ISC happen with two time constants of 304 fs and 1.1 ps. After that, the TA spectra evolve with two more time constants of 13.7 and 187 ps before establishing the final long-lived ^{3}MMLL′CT state.

In order to fully understand the excited state dynamics of **Pt-RDM3**, decay associated spectra (DAS) were generated based on global fitting (Figure 9; see full description of methodology in the Experimental Section). As seen in Figure 9, the 304 fs DAS is consistent with an ultrafast reorganization of excited

DOI: 10.1021/jacs.7b11581
J. Am. Chem. Soc. 2018, 140, 2575−2586

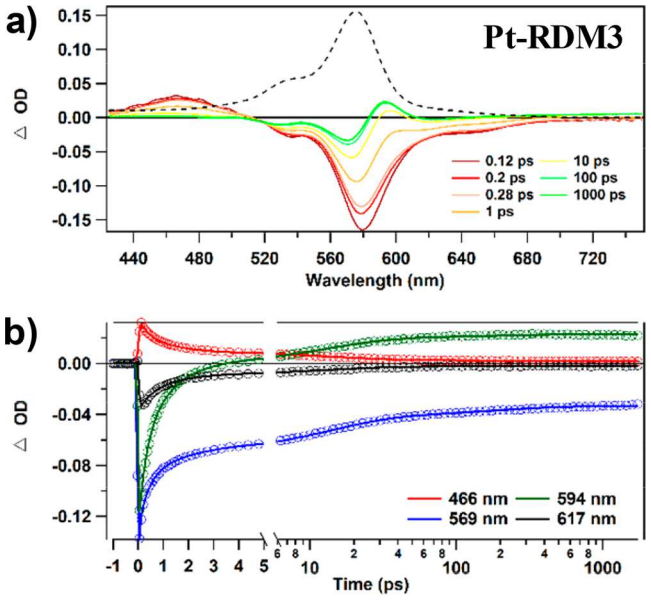

Figure 8. (a) TA spectra of **Pt-RDM3** at indicated time delays, and (b) kinetic traces of **Pt-RDM3** at selected wavelengths, in acetonitrile after pulsed laser excitation at 550 nm.

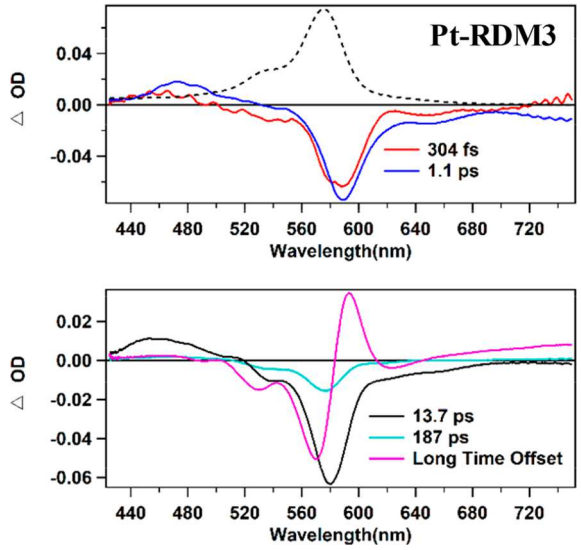

Figure 9. DAS of **Pt-RDM3** after pulsed laser excitation at 550 nm in acetonitrile. The ground state absorption spectrum is presented in the top panel as dashed lines.

states. The 1.1 ps-DAS shows a loss of rhodamine GSB, ESA and SE, therefore it is assigned to the SEnT process from rhodamine $^1\pi-\pi^*$ state to the PtN_2S_2 ^{1}MMLL′CT state. The subsequent ISC process from the ^{1}MMLL′CT state to the ^{3}MMLL′CT state is also convoluted in this 1.1 ps DAS spectrum. The 13.7 ps DAS shows a recovery of rhodamine absorption at 580 nm and PtN_2S_2 absorption from 600 to 670 nm. The feature of simultaneous recovery of *both* the rhodamine and PtN_2S_2 absorption in this DAS spectrum cannot be explained by processes involving *only* the $^1\pi-\pi^*/^3\pi-\pi^*$ and ^{1}MMLL′CT/^{3}MMLL′CT states, suggesting the participation of additional state(s) in the excited state dynamics. Based on electrochemical data, a charge separated (CS) state formulated as $RDM^{(0\bullet)}-Pt^{(+\bullet)}$ lies below the $^1\pi-\pi^*$ state in energy and the 13.7 ps DAS is indeed consistent with charge recombination of the $RDM^{(0\bullet)}-Pt^{(+\bullet)}$ state to the ^{3}MMLL′CT state. The relative energies of dyad excited states are discussed in detail below. This analysis suggests that the $RDM^{(0\bullet)}-Pt^{(+\bullet)}$ state is formed along with the SEnT process in 1.1 ps. The subsequent 187 ps DAS shows a loss of rhodamine GSB, and is attributed to triplet energy transfer (TEnT) from the $^3\pi-\pi^*$ to the ^{3}MMLL′CT state. It appears that the electronic coupling between rhodamine and the PtN_2S_2 complex is sufficient to cause both ground-state absorption bands to be bleached when the molecule occupies the $^3\pi-\pi^*$ state. During the TEnT process, the rhodamine ground-state absorption recovers while the PtN_2S_2-centered absorption remains bleached, evident in the absence of change in the 187 ps DAS after 600 nm. Finally, the last DAS that remains for the duration of the experiment exhibits the dispersive feature centered at 583 nm, and is consistent with the relaxation of the ^{3}MMLL′CT state to ground state.

The excited state dynamics of **Pt-RDM3** are summarized in Figure 10. When excited to the ^{1}MMLL′CT state, the excited

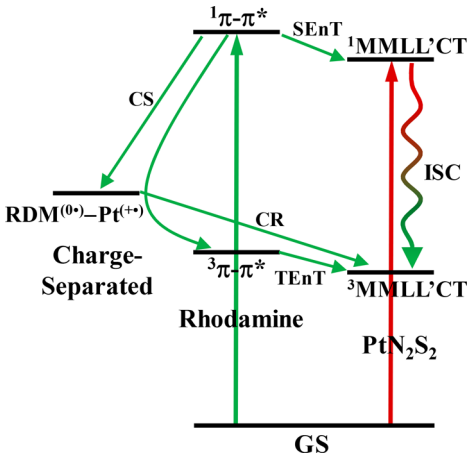

Figure 10. Excited state relaxation pathways of **Pt-RDM3** in acetonitrile when excited at 550 (green lines) and 650 nm (red lines), CR = charge recombination. ISC is labeled in both green and red because it is involved in excited state relaxation at both excitations.

states undergo an ISC process to the long-lived ^{3}MMLL′CT state before relaxing to the ground state. When excited to the rhodamine $^1\pi-\pi^*$ state, the excited state relaxation is more complex, and involves SEnT to the ^{1}MMLL′CT state, formation of the $RDM^{(0\bullet)}-Pt^{(+\bullet)}$ CS state, and population of the $^3\pi-\pi^*$ state. All three states eventually end up in the same ^{3}MMLL′CT state through ISC, charge recombination, and TEnT process, respectively, which is crucial for H_2 generation.

DISCUSSION

Despite the structural similarity of the **Pt-RDM** dyads, the H_2 production results differ significantly among the dyads. Under various experimental conditions, systems having the **Pt-RDM3** dyad always display the highest TONs for the generation of H_2, followed respectively by those of **Pt-RDM2**, and **Pt-RDM1**. To eliminate that the cause of the variation in TONs is simply due to differences in the absorbed photons for each dyad from the white LED emission light source, the absorbed photons by **Pt-RDM1−3**/Pt-TiO_2 systems were quantified. The white light LED emission profile is shown in Figure S19. The detailed method of quantification is described in the Experimental Section. Based on the calculation, the ratio of absorbed photons

DOI: 10.1021/jacs.7b11581
J. Am. Chem. Soc. 2018, 140, 2575−2586

for **Pt-RDM1**: **Pt-RDM2**: **Pt-RDM3** is 1.0:0.96:0.99, and 1.0:0.96:1.01 when the dyads in 2.5 mL of 50 μM and 10 μM solutions are attached on Pt-TiO_2, respectively (Figure S20). This means that the number of absorbed photons is roughly the same for the three **Pt-RDM** dyads and that the substantial difference in TONs for the dyads can not be explained by the differences in the photons absorbed by them.

To explain the different TONs for the **Pt-RDM** dyads, it is worth revisiting their excited state dynamics in acetonitrile. Despite the complex excited-state dynamics described above, the excited states of the three dyads all appear to relax to the ^{3}MMLL′CT state eventually, no matter whether initial excitation is to the $^1\pi-\pi^*$ or the ^{1}MMLL′CT excited state (Figures 11a, S15, and S17). Since the long-lived ^{3}MMLL′CT

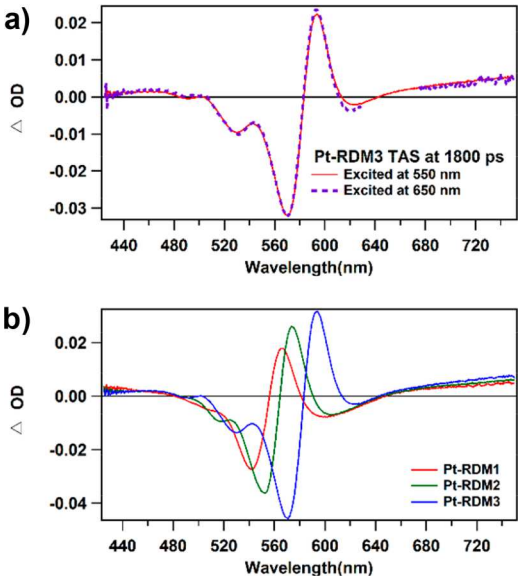

Figure 11. (a) Normalized TA spectra of **Pt-RDM3** in acetonitrile at 1800 ps delay after pulsed excitation at 550 nm (solid red) and 650 nm (dotted purple). (b) TA spectra of **Pt-RDM1** (red), **Pt-RDM2** (green), and **Pt-RDM3** (blue) at 1800 ps after pulsed excitation at 550 nm. The spectra are scaled to account for difference in absorption at the excitation wavelength.

state is responsible for electron injection into TiO_2 (and therefore H_2 generation), the efficiency of relaxation of the excited states to the ^{3}MMLL′CT state is central to understanding the relative activity of the dyad systems for H_2 generation.

Like the ^{1}MMLL′CT state, the TA spectra of the ^{3}MMLL′CT state shows a dispersive feature, consistent with a red-shift of the rhodamine ground-state absorption caused by the presence of the large excited-state dipole of the nearby PtN_2S_2 chromophore. Given the structural similarity of the **Pt-RDM** dyads, the amplitude of the dispersive feature is directly correlated with the yield of the ^{3}MMLL′CT state. A higher amplitude of the dispersive feature corresponds to a higher yield of the ^{3}MMLL′CT state, and vice versa. Figure 11b shows the TAS at 1800 ps for **Pt-RDM1**, **Pt-RDM2**, and **Pt-RDM3** after pulsed laser excitation at 550 nm. The spectrum is scaled to account for the difference in absorption at the excitation wavelength for the three dyads. After taking into account the difference in extinction coefficient of the $^1\pi-\pi^*$ absorption of **RDM1−3**, the relative amplitude of the dispersive feature indicates a ratio of ∼0.6:0.8:1 for the yield of the ^{3}MMLL′CT state for **Pt-RDM1**:**Pt-RDM2**:**Pt-RDM3**, indicating that **Pt-RDM3** has the largest triplet yield out of the three dyads. The trend in the yield of ^{3}MMLL′CT state is coincident with the TONs in H_2 production results, therefore providing a rigorous basis for the different H_2 generation activity for **Pt-RDM1**, **Pt-RDM2**, and **Pt-RDM3**.

The yield of the ^{3}MMLL′CT state is directly related to the excited state energy levels of the dyads. As shown in Figure 12,

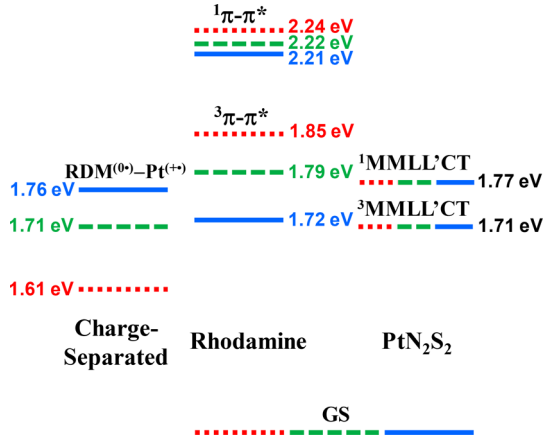

Figure 12. Energy level diagram of **Pt-RDM1** (red dotted), **Pt-RDM2** (green dashed), and **Pt-RDM3** (blue solid) in acetonitrile.

the energies of the excited states are given relative to the ground state based on experimental data. The $^1\pi-\pi^*$ excited state energies of the **Pt-RDM** dyads are taken from the intersection of the tangent line of the high-energy side of the room temperature fluorescence band with the wavenumber axis (Figure S21).[62] The $^3\pi-\pi^*$ and ^{3}MMLL′CT state energies are obtained following the same method based on the phosphorescence of the **Pt-RDM** dyads when excited at 550 and 650 nm at 77 K, respectively (Figure S6). The ^{1}MMLL′CT state energies are taken from the absorption onset of the **Pt-RDM** dyads (700 nm). The energies of the CS states are calculated using the Rehm−Weller eq (eq 1), in which $E^\circ(A/A^{\bullet-})$ represents the first reduction potential of the acceptor and $E^\circ(D^{\bullet+}/D)$ represents the first oxidation potential of the donor, and ΔG_w accounts for the Coulombic potential energy change during electron transfer, eq 2, in which r_{DA} is the distance between donor and acceptor.[63] Note that in the RDM$^{(0\bullet)}$–Pt$^{(+\bullet)}$ CS state, ΔG_w is 0, because either the rhodamine or the PtN_2S_2 moiety has zero charge before or after charge separation.[54]

$$E_{CS} = E^\circ(D^{\bullet+}/D) - E^\circ(A/A^{\bullet-}) + \Delta G_w \quad (1)$$

$$\Delta G_w = \frac{z(D^{\bullet+})z(A^{\bullet-})e^2}{4\varepsilon_0\varepsilon_r r_{DA}} - \frac{z(D)z(A)e^2}{4\varepsilon_0\varepsilon_r r_{DA}} \quad (2)$$

As seen in Figure 12, the energies of the ^{1}MMLL′CT and ^{3}MMLL′CT states remain the same for all three dyads, the rhodamine-centered $^1\pi-\pi^*$ and $^3\pi-\pi^*$ states decrease in energy, while the RDM$^{(0\bullet)}$–Pt$^{(+\bullet)}$ CS states increase in energy from **Pt-RDM1** to **Pt-RDM3**. As a result, the RDM$^{(0\bullet)}$–Pt$^{(+\bullet)}$ CS state is well below the ^{3}MMLL′CT state in **Pt-RDM1**, whereas it is isoenergetic to the ^{3}MMLL′CT state in **Pt-RDM2**, and above the ^{3}MMLL′CT state in **Pt-RDM3**. The driving force for the charge recombination from the RDM$^{(0\bullet)}$–Pt$^{(+\bullet)}$ CS state to populate the ^{3}MMLL′CT state is −0.1, 0, and 0.04

DOI: 10.1021/jacs.7b11581
J. Am. Chem. Soc. 2018, 140, 2575−2586

eV for **Pt-RDM1**, **Pt-RDM2**, and **Pt-RDM3**, respectively, making the population from the CS state to the ^{3}MMLL′CT state thermodynamically uphill in **Pt-RDM1**. In this regard, it appears likely that some portion of the excited-state population in **Pt-RDM1** and **Pt-RDM2** relaxes directly to the ground state through the RDM$^{(0\bullet)}$–Pt$^{(+\bullet)}$ state, rather than relaxation to the photochemically productive ^{3}MMLL′CT state, giving rise to lower ^{3}MMLL′CT state yields for these two dyads and hence, lower H_2 production activity. Unfortunately, the convoluted TAS kinetics with multiple excited-states dynamically evolving on many different time scales makes direct observation of the CS state formation and its recombination difficult to confirm.

CONCLUSION

Three rhodamine-PtN_2S_2 dyads, **Pt-RDM1**–**3**, have been synthesized and studied as photosensitizers for white light-driven generation of H_2 from aqueous protons. **Pt-RDM1**–**3** exhibit strong and broad absorption in the visible region of the spectrum with the major absorption characteristic of the rhodamine dye. When linked to Pt-TiO_2 via phosphonate attachment, the systems containing **Pt-RDM1**–**3** show notable activity and excellent robustness for H_2 production under white light irradiation. Within the three dyads, **Pt-RDM3** displays the highest TON, followed by **Pt-RDM2**, and then **Pt-RDM1**. Ultrafast transient absorption spectroscopy results indicate the excited states of **Pt-RDM1**–**3** relax to the same ^{3}MMLL′CT state of the PtN_2S_2 chromophore, regardless of whether the excitation is to the rhodamine $^1\pi$–π^* state or the PtN_2S_2 ^{1}MMLL′CT state. The yield of the ^{3}MMLL′CT state decreases progressively in going from **Pt-RDM3** to **Pt-RDM1**, due to a charge separated state, RDM$^{(0\bullet)}$-Pt$^{(+\bullet)}$, that delivers some of the excited state population to ground state in **Pt-RDM1** and **Pt-RDM2**. The trend in ^{3}MMLL′CT state yield correlates well with that in H_2 generation, providing a viable explanation for highest H_2 production activity observed for the **Pt-RDM3** photosensitized system. This study highlights the importance of excited state dynamics in dyad photosensitizers based on linked light absorber-charge transfer moieties in effecting photochemical generation of H_2 and represents a new path for exploring rhodamine dyes as antennas for light-driven electron transfer applications.

EXPERIMENTAL SECTION

Materials. Acetonitrile (Fisher Chemical, HPLC grade), dichloromethane (Fisher Chemical, >99.9%), methanol (Fisher Chemical, >99.9%), acetone (Fisher Chemical, 99.7%), sulfuric acid (H_2SO_4, J.T.Baker, 93%), 3-(dimethylamino)phenol (TCI, >97%), 8-hydroxyjulolidine (TCI, >97%), 1-methyl-1,2,3,4-tetrahydroquinolin-7-amine hydrochloride (Oxchem, >95.0%), p-chloranil (Alfa Aesar, 97.0%), potassium hydroxide (KOH, Mallinckrodt, 87.8%), sodium hydroxide (NaOH, Fisher Chemical, 99.3%), ammonium hexafluorophosphate (NH_4PF_6, Sigma-Aldrich, >98.0%), tetrabutylammonium hexafluorophosphate (TBAPF_6, Sigma-Aldrich, >99.0%), anhydrous magnesium sulfate ($MgSO_4$, Fisher Chemical), potassium *tert*-butoxide (Sigma-Aldrich, >98.0%), and ascorbic acid (AA, EMD Chemicals, >99.0%) were used as received. 2-Oxobenzo[*D*][1,3]dithiole-5-carbaldehyde,[64] 7-hydroxy-1-methyl-1,2,3,4-tetrahydroquinolin,[65] Pt(Pbpy)$_2$Cl$_2$[46] (Pbpy = 4,4′-bis(diethylphosphonate)-2,2′-bipyridine), and Pt-TiO_2 nanoparticles (Pt: 0.5% in wt) were synthesized following literature procedures.[46]

Synthesis. *General Procedure for the Preparation of Rhodamine Dyes.* One equivalent of 2-oxobenzo[*d*][1,3]dithiole-5-carbaldehyde and 2 equiv of the corresponding 3-amino-phenol were dissolved in 10 mL of dichloromethane, and the solvent was removed on rotary evaporator before 10 mL ice cold 60% H_2SO_4 was added. The mixture was stirred until the solid was fully dissolved, and the solution was heated at 85 °C for 18 h. The reaction mixture was cooled to room temperature before 2 equiv of p-chloranil was added, and the mixture was stirred for another 1 h at room temperature. After that, the pH of the solution was adjusted to pH = 7 using 10 M KOH aqueous solution. The mixture was extracted with dichloromethane (30 mL × 3), dried with anhydrous $MgSO_4$, and concentrated to dryness on rotary evaporator. The crude product was loaded onto a silica gel column using dichloromethane/MeOH = 15:1 (v:v) as eluent. After removing a fast-moving dark brown impurity, the eluent was changed to dichloromethane/MeOH = 8:1 (v:v) and the long bright orange/red band comprising three to four different bands were collected altogether. The solvent was removed, and the solid was redissolved in minimum amount of MeOH, followed by the addition of 3 equiv of NH_4PF_6 in 2 mL of DI water. The afforded suspension was stirred for 30 min, filtered through a medium frit, rinsed thoroughly with DI water, and dried in vacuo. The solid was purified by a silica gel column using dichloromethane/MeOH = 20:1 (v:v) as eluent. The first red orange band was collected, concentrated to dryness to afford the desired product as purple or blue solid.

RDM1. For **RDM1**, 153 mg of the 2-oxobenzo[*d*][1,3]dithiole-5-carbaldehyde (0.78 mmol) and 215 mg of 3-(dimethylamino)phenol (1.57 mmol) were dissolved in 10 mL of ice cold 60% H_2SO_4; 155 mg of **RDM1** was obtained as a purple solid. Yield = 34%. ^{1}H NMR (400 MHz, $CDCl_3$) δ 7.77 (d, J = 8.1 Hz, 1H), 7.56 (s, 1H), 7.41 (d, J = 7.2 Hz, 1H), 7.35 (d, J = 9.5 Hz, 2H), 6.93 (d, J = 9.4 Hz, 2H), 6.88 (s, 2H), 3.33 (s, 12H). ESI-MS: m/z = 433.7 (calcd. for $[C_{24}H_{21}N_2S_2O_2]^+$: 433.6).

RDM2. For **RDM2**, 100 mg of the 2-oxobenzo[*d*][1,3]dithiole-5-carbaldehyde (0.51 mmol) and 165 mg of 7-hydroxy-1-methyl-1,2,3,4-tetrahydroquinolin (1.02 mmol) were dissolved in 10 mL of ice cold 60% H_2SO_4; 255 mg of **RDM2** was obtained as a purple solid. Yield = 80%. ^{1}H NMR (500 MHz, $CDCl_3$) δ 7.79 (d, J = 8.1 Hz, 1H), 7.50 (s, 1H), 7.37 (d, J = 8.1 Hz, 1H), 6.89 (s, 2H), 6.71 (s, 2H), 3.59 (t, J = 5.5 Hz, 4H), 3.25 (s, 6H), 2.80–2.68 (m, 4H), 2.04–1.93 (m, 4H). ESI-MS: m/z = 485.8 (calcd. for $[C_{28}H_{25}N_2S_2O_2]^+$: 485.7).

RDM3. For **RDM3**, 60 mg of the 2-oxobenzo[*d*][1,3]dithiole-5-carbaldehyde (0.30 mmol) and 116 mg of 8-hydroxyjulolidine (1.57 mmol) were dissolved in 10 mL of ice cold 60% H_2SO_4; 119 mg of **RDM3** was obtained as a blue solid. Yield = 58%. ^{1}H NMR (400 MHz, $CDCl_3$) δ 7.75 (d, J = 8.1 Hz, 1H), 7.45 (s, 1H), 7.32 (d, J = 8.1 Hz, 1H), 6.75 (s, 2H), 3.57–3.49 (m, 4H), 3.04 (t, J = 6.2 Hz, 2H), 2.72 (t, J = 5.9 Hz, 2H), 2.13–2.06 (m, 2H), 2.03–1.94 (m, 2H). ESI-MS: m/z = 537.8 (calcd. for $[C_{32}H_{29}N_2S_2O_2]^+$: 537.7).

General Procedure for the Preparation of the Pt-RDM Dyads. The rhodamine dye and 1 equiv of potassium *tert*-butoxide were dissolved in anhydrous MeOH under N_2 atmosphere. After stirring for 15 min at room temperature, 1 equiv of Pt(Pbpy)Cl_2 was added and the mixture was left to stir under N_2 for 24 h at room temperature. The solvent was removed on a rotary evaporator, and the crude product was purified by column chromatography using dichloromethane:acetone = 7:1 (v:v) as eluent. After removing a bright orange band, the purple product was collected. The solvent was removed to afford the product as a purple solid.

Pt-RDM1. For **Pt-RDM1**, 100 mg of **RDM1** (0.17 mmol), 39 mg of *tert*-butoxide (0.35 mmol), and 120 mg of Pt(Pbpy)Cl_2 (0.17 mmol) were dissolved in 20 mL of anhydrous MeOH, and 100 mg of product was obtained. Yield = 49%. ^{1}H NMR (500 MHz, $CDCl_3$) δ 9.52 (s, 1H), 9.45 (s, 1H), 8.55 (d, J = 13.5 Hz, 2H), 7.91–7.86(m, 2H), 7.63 (d, J = 8.1 Hz, 1H), 7.58 (d, J = 9.4 Hz, 2H), 7.43 (s, 1H), 6.87–6.83(m, 5H), 4.35–4.21 (m, 8H), 3.31 (s, 12H), 1.42 (q, J = 7.0 Hz, 12H). ESI-MS: m/z = 1029.0 (calcd. for $[PtC_{41}H_{47}N_4S_2O_7P_2]^+$: 1029.2). Elemental Analysis: calcd. (found) for $PtC_{43}H_{51}N_4S_2O_7P_3F_6Cl_4$ (**Pt-RDM1**·2CH_2Cl_2), %: C, 38.43 (38.02); H, 3.83 (3.78); N, 4.17 (4.09).

Pt-RDM2. For **Pt-RDM2**, 60 mg of **RDM2** (0.095 mmol), 22 mg of *tert*-butoxide (0.20 mmol), and 65 mg of Pt(Pbpy)Cl_2 (0.095 mmol) were dissolved in 10 mL of anhydrous MeOH, and 30 mg of product was collected. Yield = 26%. ^{1}H NMR (400 MHz, $CDCl_3$) ^{1}H NMR (500 MHz, $CDCl_3$) δ 9.61–9.41 (m, 2H), 8.57 (d, J = 13.7 Hz, 2H),

DOI: 10.1021/jacs.7b11581
J. Am. Chem. Soc. 2018, 140, 2575–2586

7.91−7.84 (m, 2H), 7.63 (d, J = 7.9 Hz, 1H), 7.39 (d, J = 1.7 Hz, 1H), 7.14 (s, 2H), 6.81 (dd, J = 7.9, 1.8 Hz, 1H), 6.70 (s, 2H), 4.40−4.17 (m, 8H), 3.58 (t, J = 5.9 Hz, 4H), 3.24 (s, 6H), 2.72 (t, J = 5.9 Hz, 4H), 2.04−1.93 (m, 4H), 1.42 (q, J = 7.0 Hz, 12H). ESI-MS: m/z = 1081.1 (calcd. for $[PtC_{45}H_{51}N_4S_2O_7P_2]^+$: 1081.3). Elemental Analysis: calcd. (found) for $PtC_{47}H_{55}N_4S_2O_7P_3F_6Cl_4$ (**Pt-RDM2**·$2CH_2Cl_2$), %: C, 40.44 (39.96); H, 3.97 (4.02); N, 4.01 (3.83).

Pt-RDM3. For **Pt-RDM3**, 100 mg of **RDM3** (0.15 mmol), 34 mg of *tert*-butoxide (0.30 mmol), and 102 mg of Pt(Pbpy)Cl_2 (0.15 mmol) were dissolved in 20 mL of anhydrous MeOH, and 53 mg of product was collected. Yield = 28%. ^{1}H NMR (400 MHz, $CDCl_3$) δ 9.52−9.47 (m, 2H), 8.55 (d, J = 13.6 Hz, 2H), 7.91−7.83(m, 2H), 7.60 (d, J = 8.0 Hz, 1H), 7.34 (s, 1H), 7.01 (s, 2H), 6.76 (d, J = 8.0 Hz, 1H), 4.35−4.20 (m, 8H), 3.55−3.47 (m, 8H), 3.03 (t, J = 6.1 Hz, 4H), 2.69 (d, J = 5.8 Hz, 4H), 2.13−2.08 (m, 4H), 2.00−1.94 (m, 4H), 1.41 (q, J = 6.9 Hz, 12H). ESI-MS: m/z = 1133.2 (calcd. for $[PtC_{49}H_{55}N_4S_2O_7P_2]^+$: 1133.4). Elemental Analysis: calcd. (found) for $PtC_{51}H_{59}N_4S_2O_7P_3F_6Cl_4$ (**Pt-RDM3**·$2CH_2Cl_2$), %: C, 42.30 (42.06); H, 4.11 (4.28); N, 3.87 (3.86).

Characterization. ^{1}H NMR spectra were recorded on a Bruker Avance 500-MHz spectrometer and referenced to the residual ^{1}H in $CDCl_3$ solvent. Elemental analyses were performed using a PerkinElmer 2400 Series II Analyzer. Mass spectrometry was performed on a Shimadzu LCMS and an LTQ VELOS Thermo LCMS (positive mode). UV−vis absorption spectra were recorded on a Cary 60 UV−vis spectrophotometer, using a 1 cm path length quartz cuvette. Electrochemical measurements were performed with a CHI 680D potentiostat in an Ar-purged acetonitrile solution, using a platinum disk working electrode, a platinum-wire auxiliary electrode, and a saturated calomel reference electrode. Ferrocene was added as an internal reference. All measurements were performed with 0.1 V/s scan rate using 0.1 M $TBAPF_6$ as the supporting electrolyte.

Steady-State Photoluminescence. Steady-state photoluminescence spectra were recorded on a Spex Fluoromax-P fluorometer and corrected for instrument response. The intensity was integrated for 0.1 s at 1 nm resolution and averaged over 3 scans. All solutions were purged with N_2 for 20 min prior to measurements. Quantum yields were measured using $[Ru(bpy)_3](PF_6)_2$ in acetonitrile as the standard (φ_{PL} = 0.062) with the optically dilute method.[66] The photoluminescence spectra at 77 K were collected in a liquid N_2-frozen optical glass (EtOH/MeOH = 4:1 (v:v)).

Ultrafast Transient Absorption. The instrumentation for this experiment has been described elsewhere.[67] In brief, pump pulses were produced from a home-built noncollinear parametric amplifier (NOPA) centered at 550 and 650 nm with a pulse energy of 80 and 100 nJ per pulse, respectively. The pulse spectrum was measured to have a fwhm of 12 and 14 nm for 550 and 650 nm, respectively.[68,69] The probe beam was created by focusing of the fundamental 800 nm beam through a sapphire crystal to produce a white light continuum spanning 425−785 nm. The white light spectrum was filtered using a dye solution (NIR800A, QCR Solutions Corp) to block residual 800 nm light by placing it in the white light path before the sample. Solution samples with an absorbance of ∼0.1−1.1 at the pump wavelength were prepared in a 2 mm fused-silica cuvette, purged with argon for 20 min and sealed with an airtight septa. The samples were translated vertically at ∼2 mm/s to refresh the illuminated area. Absorption spectra were obtained after each experiment to ensure that no degradation occurred during the experiment. TA signals were collected at magic angle polarization via rotating the pump pulse polarization 54.7° from that of the probe.

Global fitting was performed using the Glotaran software package.[70] The kinetics were modeled as a convolution of the Gaussian instrument response function with a linear combination of n exponential functions with wavelength dependent amplitudes:

$$I(t, \lambda) = \sum_{i=1}^{n} A_i(\lambda) \exp -(t/\tau_i) \quad (3)$$

The decay associated spectra, $A_i(\lambda)$, correspond to the amplitude of transient absorption change occurring with each time-constant, τ_i, and can be used to decipher what photophysical relaxation is occurring with that time-constant. Coherent artifacts around Δt = 0 were fit by including short duration spikes in the fit. The long-time offset signal was modeled as an exponential with a fixed 1 μs time constant to accommodate for a long-lasting triplet that shows no loss in amplitude for the duration of the experiment (1.8 ns). Fitting of single wavelength kinetics was also performed with a series of exponentials convoluted with the instrument response function (IRF). The IRF was determined from optical Kerr effect (OKE) signals obtained with a 1 mm glass slide and found to be 100 fs for both excitation wavelengths.

Attachment of Dyad on Pt-TiO_2 Nanoparticle. Pt-TiO_2 nanoparticles were normally stored at 80 °C in an oven to stay dry. Here, 20 mg of Pt-TiO_2 nanoparticles was mixed with 2.5 mL of X μM (X = 50, 10) dyad solution in acetonitrile at room temperature. The suspension was sonicated for 10 min in the dark, before storing in the dark overnight. The colored dyad-attached Pt-TiO_2 particles were collected by centrifugation at 7500 rpm for 10 min. UV−vis absorption of the supernatant was measured to quantify the amount of dye attachment. After drying in the air, to the dyad-attached Pt-TiO_2 nanoparticles was added 5 mL of X M (X = 0.5, 1.0) AA aqueous solution (pH = 4.0), the suspension was sonicated for 1 min and transferred to a 40 mL glass vial. After that, the suspension was sonicated for an additional 3 min prior to being placed in the photochemical H_2 production setup.

Replenishment of AA Aqueous Solution. After 40 h of light-driven H_2 production, the suspension was transferred to a centrifuge tube and centrifuged at 7500 rpm for 10 min. The used AA aqueous solution supernatant was removed using a pipet, and the dyad-attached Pt-TiO_2 nanoparticles were rinsed with CH_3CN. Following centrifugation (7500 rpm for 10 min), the dyad-attached Pt-TiO_2 nanoparticles were then air-dried. To these nanoparticles was added 5 mL of either 0.5 or 1.0 M AA aqueous solution (pH = 4.0), and the suspension was transferred to a 40 mL glass vial for another round of light-driven H_2 production.

Light-Driven H_2 Production. The 40 mL sample vials (Figure S9) were placed in a temperature-controlled block at 15 °C and each vial was sealed with an airtight cap fitted with a pressure transducer and a rubber septum. The samples were then purged with a mixture of gas containing N_2/CH_4 (79:21 mol %). The methane present in the gas mixture serves as an internal reference for GC analysis at the end of the experiment. The samples were irradiated in a customized 16-well photolysis apparatus with Philips LumiLEDs Luxeon ES Cool White (400−800 nm) 700 mA LEDs from underneath, mounted on a 20 mm Star CoolBase atop an orbital shaker. The light power of each LED was set to 300 mW and measured with an L30 A thermal sensor and a Nova II power meter (Ophir- Spiricon). The light was irradiated on an area of ∼5 cm^2, corresponding to a light intensity of (∼60 mW/cm^2). The pressure changes in the vials were recorded using a Labview program from a Freescale semiconductor sensor (MPX4259A series). At the end of the experiment, the headspaces of the vials were characterized by gas chromatography to ensure that the measured pressure change was a consequence of hydrogen generation and to confirm the amount of hydrogen generated. The amounts of hydrogen evolved were determined using a Shimadzu GC-17A gas chromatograph with a 5 Å molecular sieve column (30 m, 0.53 mm) and a thermal conductivity detector and were quantified by a calibration plot to the internal CH_4 standard.

Quantification of Absorbed Photons. The emission profile of the white light LED which was measured using a fiber optics (Ocean Optics USB4000 with a CCD diode array detector) is shown in Figure S19. The absorbed photons of the dyad-attached Pt-TiO_2 nanoparticles in 5 mL of AA aqueous solution were calculated at each wavelength using the following equations:

$$\text{absorbed photons}(\lambda) = \text{LED emission profile}(\lambda) \times \text{absorptance}(\lambda)$$

DOI: 10.1021/jacs.7b11581
J. Am. Chem. Soc. 2018, 140, 2575−2586

$$\text{absorptance}\ (\lambda) = 1 - 10^{-\text{Abs}(\lambda)};$$

$$\text{Abs}(\lambda) = \varepsilon(\lambda) \times \text{concentration} \times \text{pathlength}$$

The path length was ~1 cm (Figure S9) when 5 mL of AA was present. The concentrations of the TiO_2-bound dyad are estimated as 25 and 5 μM based on the use of 2.5 mL of 50 and 10 μM dyad solutions for attachment to Pt-TiO_2. UV−vis spectra of these solutions after centrifugation to remove the dyad-bound-Pt-TiO_2 indicated essentially quantitative dyad binding to TiO_2. The extinction coefficient of the dyad in acetonitrile was used as a close estimate for that of the dyad on Pt-TiO_2. Absorptance describes the fraction of absorbed light at a specific wavelength.[71] The respective absorptance of 25 and 5 μM **Pt-RDM1−3** dyads are shown in Figure S20a and c, and the corresponding absorbed photons are shown in Figure S20b and d. The total number of absorbed photons for each dyad was obtained by integrating the area underneath the curve in Figure S20b and d.

■ ASSOCIATED CONTENT

Supporting Information

The Supporting Information is available free of charge on the ACS Publications website at DOI: 10.1021/jacs.7b11581.

^{1}H NMR spectra of **RDM1−3** and **Pt-RDM1−3** in $CDCl_3$; UV−vis absorption of **Pt-RDM1** and **Pt-RDM3** in dichloromethane; PL quenching of **Pt-RDM2** and **Pt-RDM3** in acetonitrile; Phosphorescence of **Pt-RDM1−3** at 77 K upon 550 or 650 nm light excitation; UV−vis absorption spectra of 50 μM dyad in acetonitrile before and after adsorption on Pt-TiO_2; dyad-attached Pt-TiO_2 nanoparticles in 5 mL of 1.0 M AA aqueous solution before and after photochemical H_2 production; GC calibration curve to calculate the amount of H_2 produced; AA aqueous solution after H_2 production; GC analysis of the headspace gas atmosphere after photochemical H_2 production; TA spectra of **RDM1** and **RDM2** after pulsed 550 nm laser excitation; TA spectra and DAS of **Pt-RDM1** and **Pt-RDM2** after pulsed 550 or 650 nm laser excitation; emission profile of the white light LED; quantification of absorbed photons for **Pt-RDM1−3** on Pt-TiO_2; determination of E_{0-0} (PDF)

■ AUTHOR INFORMATION

Corresponding Authors

*david.mccamant@rochester.edu

*richard.eisenberg@rochester.edu

ORCID

Guocan Li: 0000-0003-1188-4887

Hongjin Lv: 0000-0002-9212-7572

David W. McCamant: 0000-0002-9095-040X

Richard Eisenberg: 0000-0003-1762-535X

Notes

The authors declare no competing financial interest.

■ ACKNOWLEDGMENTS

This work was supported by the National Science Foundation Collaborative Research Grant CHE-1151789.

■ REFERENCES

(1) Bard, A. J.; Fox, M. A. *Acc. Chem. Res.* **1995**, *28*, 141−145.

(2) Lewis, N. S.; Nocera, D. G. *Proc. Natl. Acad. Sci. U. S. A.* **2006**, *103*, 15729−15735.

(3) Gray, H. B. *Nat. Chem.* **2009**, *1*, 7.

(4) Meyer, T. J. *Acc. Chem. Res.* **1989**, *22*, 163−170.

(5) Esswein, A. J.; Nocera, D. G. *Chem. Rev.* **2007**, *107*, 4022−4047.

(6) Brennaman, M. K.; Dillon, R. J.; Alibabaei, L.; Gish, M. K.; Dares, C. J.; Ashford, D. L.; House, R. L.; Meyer, G. J.; Papanikolas, J. M.; Meyer, T. J. *J. Am. Chem. Soc.* **2016**, *138*, 13085−13102.

(7) Han, Z. J.; Qiu, F.; Eisenberg, R.; Holland, P. L.; Krauss, T. D. *Science* **2012**, *338*, 1321−1324.

(8) Lv, H.; Ruberu, T. P. A.; Fleischauer, V. E.; Brennessel, W. W.; Neidig, M. L.; Eisenberg, R. *J. Am. Chem. Soc.* **2016**, *138*, 11654−11663.

(9) Khnayzer, R. S.; Thoi, V. S.; Nippe, M.; King, A. E.; Jurss, J. W.; El Roz, K. A.; Long, J. R.; Chang, C. J.; Castellano, F. N. *Energy Environ. Sci.* **2014**, *7*, 1477−1488.

(10) Han, Z. J.; Eisenberg, R. *Acc. Chem. Res.* **2014**, *47*, 2537−2544.

(11) Chen, Z.; Concepcion, J. J.; Jurss, J. W.; Meyer, T. J. *J. Am. Chem. Soc.* **2009**, *131*, 15580−15581.

(12) Khnayzer, R. S.; McCusker, C. E.; Olaiya, B. S.; Castellano, F. N. *J. Am. Chem. Soc.* **2013**, *135*, 14068−14070.

(13) Elgrishi, N.; McCarthy, B. D.; Rountree, E. S.; Dempsey, J. L. *ACS Catal.* **2016**, *6*, 3644−3659.

(14) Helm, M. L.; Stewart, M. P.; Bullock, R. M.; DuBois, M. R.; DuBois, D. L. *Science* **2011**, *333*, 863−866.

(15) Karunadasa, H. I.; Montalvo, E.; Sun, Y.; Majda, M.; Long, J. R.; Chang, C. J. *Science* **2012**, *335*, 698−702.

(16) Zee, D. Z.; Chantarojsiri, T.; Long, J. R.; Chang, C. J. *Acc. Chem. Res.* **2015**, *48*, 2027−2036.

(17) Eckenhoff, W. T.; Eisenberg, R. *Dalton Trans.* **2012**, *41*, 13004−13021.

(18) Hunter, B. M.; Gray, H. B.; Müller, A. M. *Chem. Rev.* **2016**, *116*, 14120−14136.

(19) Blakemore, J. D.; Crabtree, R. H.; Brudvig, G. W. *Chem. Rev.* **2015**, *115*, 12974−13005.

(20) Concepcion, J. J.; Tsai, M. K.; Muckerman, J. T.; Meyer, T. J. *J. Am. Chem. Soc.* **2010**, *132*, 1545−1557.

(21) Artero, V.; Saveant, J. M. *Energy Environ. Sci.* **2014**, *7*, 3808−3814.

(22) Kirch, M.; Lehn, J. M.; Sauvage, J. P. *Helv. Chim. Acta* **1979**, *62*, 1345−1384.

(23) Kiwi, J.; Gratzel, M. *Nature* **1979**, *281*, 657−658.

(24) Kirch, W.; Kohler, H.; von Gizycki, C. *Arch. Toxicol., Suppl.* **1979**, *62*, 359−363.

(25) Moradpour, A.; Amouyal, E.; Keller, P.; Kagan, H. *Nouv. J. Chim.* **1978**, *2*, 547−549.

(26) Lehn, J. M.; Sauvage, J. P. *Nouv. J. Chim.* **1977**, *1*, 449−451.

(27) Grätzel, M. *Acc. Chem. Res.* **1981**, *14*, 376−384.

(28) O'Regan, B.; Grätzel, M. *Nature* **1991**, *353*, 737−740.

(29) Gross, M. A.; Reynal, A.; Durrant, J. R.; Reisner, E. *J. Am. Chem. Soc.* **2014**, *136*, 356−366.

(30) Porras, J. A.; Mills, I. N.; Transue, W. J.; Bernhard, S. *J. Am. Chem. Soc.* **2016**, *138*, 9460−9472.

(31) Goldsmith, J. I.; Hudson, W. R.; Lowry, M. S.; Anderson, T. H.; Bernhard, S. *J. Am. Chem. Soc.* **2005**, *127*, 7502−7510.

(32) Lentz, C.; Schott, O.; Auvray, T.; Hanan, G.; Elias, B. *Inorg. Chem.* **2017**, *56*, 10875−10881.

(33) Jarosz, P.; Du, P. W.; Schneider, J.; Lee, S. H.; McCamant, D.; Eisenberg, R. *Inorg. Chem.* **2009**, *48*, 9653−9663.

(34) Du, P. W.; Schneider, J.; Jarosz, P.; Zhang, J.; Brennessel, W. W.; Eisenberg, R. *J. Phys. Chem. B* **2007**, *111*, 6887−6894.

(35) Du, P.; Schneider, J.; Fan, L.; Zhao, W.; Patel, U.; Castellano, F. N.; Eisenberg, R. *J. Am. Chem. Soc.* **2008**, *130*, 5056−5058.

(36) Cummings, S. D.; Eisenberg, R. *J. Am. Chem. Soc.* **1996**, *118*, 1949−1960.

(37) Hissler, M.; McGarrah, J. E.; Connick, W. B.; Geiger, D. K.; Cummings, S. D.; Eisenberg, R. *Coord. Chem. Rev.* **2000**, *208*, 115−137.

(38) Zuleta, J. A.; Burberry, M. S.; Eisenberg, R. *Coord. Chem. Rev.* **1990**, *97*, 47−64.

(39) Geary, E. A. M.; Yellowlees, L. J.; Jack, L. A.; Oswald, I. D. H.; Parsons, S.; Hirata, N.; Durrant, J. R.; Robertson, N. *Inorg. Chem.* **2005**, *44*, 242−250.

DOI: 10.1021/jacs.7b11581
J. Am. Chem. Soc. 2018, 140, 2575−2586

(40) Zhang, J.; Du, P. W.; Schneider, J.; Jarosz, P.; Eisenberg, R. *J. Am. Chem. Soc.* **2007**, *129*, 7726−7727.
(41) Mathew, S.; Yella, A.; Gao, P.; Humphry-Baker, R.; Curchod, B. F. E.; Ashari-Astani, N.; Tavernelli, I.; Rothlisberger, U.; Nazeeruddin, Md. K.; Grätzel, M. *Nat. Chem.* **2014**, *6*, 242−247.
(42) Pitre, S. P.; McTiernan, C. D.; Scaiano, J. C. *ACS Omega* **2016**, *1*, 66−76.
(43) Romero, N. A.; Nicewicz, D. A. *Chem. Rev.* **2016**, *116*, 10075−10166.
(44) Lazarides, T.; McCormick, T. M.; Wilson, K. C.; Lee, S.; McCamant, D. W.; Eisenberg, R. *J. Am. Chem. Soc.* **2011**, *133*, 350−364.
(45) Sabatini, R. P.; Zheng, B.; Fu, W. F.; Mark, D. J.; Mark, M. F.; Hillenbrand, E. A.; Eisenberg, R.; McCamant, D. W. *J. Phys. Chem. A* **2014**, *118*, 10663−10672.
(46) Zheng, B.; Sabatini, R. P.; Fu, W. F.; Eum, M. S.; Brennessel, W. W.; Wang, L. D.; McCamant, D. W.; Eisenberg, R. *Proc. Natl. Acad. Sci. U. S. A.* **2015**, *112*, E3987−E3996.
(47) Ho, P.-Y.; Zheng, B.; Mark, D.; Wong, W.-Y.; McCamant, D. W.; Eisenberg, R. *Inorg. Chem.* **2016**, *55*, 8348−8358.
(48) Chen, X.; Pradhan, T.; Wang, F.; Kim, J. S.; Yoon, J. *Chem. Rev.* **2012**, *112*, 1910−1956.
(49) Yang, Y.; Zhao, Q.; Feng, W.; Li, F. *Chem. Rev.* **2013**, *113*, 192−270.
(50) Sun, Y.-Q.; Liu, J.; Lv, X.; Liu, Y.; Zhao, Y.; Guo, W. *Angew. Chem., Int. Ed.* **2012**, *51*, 7634−7636.
(51) Wu, L.; Burgess, K. *J. Org. Chem.* **2008**, *73*, 8711−8718.
(52) Calitree, B. D.; Detty, M. R. *Synlett* **2010**, *2010*, 89−92.
(53) Jiao, G.-S.; Castro, J. C.; Thoresen, L. H.; Burgess, K. *Org. Lett.* **2003**, *5*, 3675−3677.
(54) Mani, T.; Niedzwiedzki, D. M.; Vinogradov, S. A. *J. Phys. Chem. A* **2012**, *116*, 3598−3610.
(55) Guttentag, M.; Rodenberg, A.; Kopelent, R.; Probst, B.; Buchwalder, C.; Brandstätter, M.; Hamm, P.; Alberto, R. *Eur. J. Inorg. Chem.* **2012**, *2012*, 59−64.
(56) Bachmann, C.; Probst, B.; Guttentag, M.; Alberto, R. *Chem. Commun.* **2014**, *50*, 6737−6739.
(57) Bae, E.; Choi, W. *J. Phys. Chem. B* **2006**, *110*, 14792−14799.
(58) Sabatini, R. P.; Eckenhoff, W. T.; Orchard, A.; Liwosz, K. R.; Detty, M. R.; Watson, D. F.; McCamant, D. W.; Eisenberg, R. *J. Am. Chem. Soc.* **2014**, *136*, 7740−7750.
(59) Li, Q.; Che, Y.; Ji, H.; Chen, C.; Zhu, H.; Ma, W.; Zhao, J. *Phys. Chem. Chem. Phys.* **2014**, *16*, 6550−6554.
(60) Ho, P. Y.; Wang, Y.; Yiu, S. C.; Yu, W. H.; Ho, C. L.; Huang, S. *Org. Lett.* **2017**, *19*, 1048−1051.
(61) Tan, J. L.; Yang, T. T.; Liu, Y.; Zhang, X.; Cheng, S. J.; Zuo, H.; He, H. *Luminescence* **2016**, *31*, 865−870.
(62) Garakyaraghi, S.; Crapps, P. D.; McCusker, C. E.; Castellano, F. N. *Inorg. Chem.* **2016**, *55*, 10628−10636.
(63) Weller, A. *Z. Phys. Chem.* **1982**, *133*, 93−98.
(64) Ishikawa, Y.; Miyamoto, T.; Yoshida, A.; Kawada, Y.; Nakazaki, J.; Izuoka, A.; Sugawara, T. *Tetrahedron Lett.* **1999**, *40*, 8819−8822.
(65) Chen, J.; Liu, W.; Zhou, B.; Niu, G.; Zhang, H.; Wu, J.; Wang, Y.; Ju, W.; Wang, P. *J. Org. Chem.* **2013**, *78*, 6121−6130.
(66) Caspar, J. V.; Meyer, T. J. *J. Am. Chem. Soc.* **1983**, *105*, 5583−5590.
(67) Sabatini, R. P.; Zheng, B.; Fu, W.-F.; Mark, D. J.; Mark, M. F.; Hillenbrand, E. A.; Eisenberg, R.; McCamant, D. W. *J. Phys. Chem. A* **2014**, *118*, 10663−10672.
(68) Cerullo, G.; Nisoli, M.; Stagira, S.; De Silvestri, S. *Opt. Lett.* **1998**, *23*, 1283−1285.
(69) Cerullo, G.; De Silvestri, S. *Rev. Sci. Instrum.* **2003**, *74*, 1−18.
(70) Snellenburg, J. J.; Laptenok, S. P.; Seger, R.; Mullen, K. M.; van Stokkum, I. H. M. *J. Stat. Softw.* **2012**, *49*, 1−22.
(71) Ardo, S.; Meyer, G. J. *Chem. Soc. Rev.* **2009**, *38*, 115−164.

DOI: 10.1021/jacs.7b11581
J. Am. Chem. Soc. 2018, 140, 2575−2586